

# Structural and Fractal Properties of Particles Emitted from Spark Ignition Engines

RAJAN K. CHAKRABARTY,\*

HANS MOOSMÜLLER,

W. PATRICK ARNOTT,†

MARK A. GARRO,‡ AND JOHN WALKER§

Desert Research Institute, Nevada System of Higher Education,  
Reno, Nevada

Size, morphology, and microstructure of particles emitted from one light-duty passenger vehicle (Buick Century; model year 1990; PM (particulate matter) mass emission rate 3.1 mg/km) and two light-duty trucks (Chevrolet C2; model year 1973; PM mass emission rate 282 mg/km, and Chevrolet El Camino; model year 1976; PM mass emission rate 31 mg/km), running California's unified driving cycles (UDC) on a chassis dynamometer, were studied using scanning electron microscopy (SEM). SEM images yielded particle properties including three-dimensional density fractal dimensions, monomer and agglomerate number size distributions, and three different shape descriptors, namely aspect ratio, root form factor, and roundness. The density fractal dimension of the particles was between 1.7 and 1.78, while the number size distribution of the particles placed the majority of the particles in the accumulation mode (0.1–0.3  $\mu\text{m}$ ). The shape descriptors were found to decrease with increasing particle size. Partial melting of particles, a rare and previously unreported phenomenon, was observed upon exposure of particles emitted during phase 2 of the UDC to the low accelerating voltage electron beam of the SEM. The rate of melting was quantified for individual particles, establishing a near linear relationship between the melting rate and the organic carbon 1 to elemental carbon ratio.

## 1. Introduction

Recent studies suggest that emissions from SI (spark ignition) vehicles are a major source of fine and ultrafine PM (particulate matter) in the atmosphere (1). Physical, chemical, and toxic properties of PM emitted into the atmosphere are of great interest because of their influence on human health (2), the earth's radiation balance and climate (3), visibility (4), and atmospheric chemistry (5). Unfortunately, very little information is available on the properties of SI PM.

While SI PM mass emission rates are much lower than those of diesel vehicles, total SI VKT (vehicle kilometer traveled) are much higher, and total PM mass emissions from all SI vehicles in the U.S. may be comparable to that from all diesel vehicles (6). Properly functioning current technology

SI vehicles emit PM mostly during cold start and hard acceleration (7). While there are numerous parameters related to engine and catalyst operation and fuel and lubricating oil composition that affect the emission of PM from SI vehicles, the primary parameter determining PM emission rates and size distributions is the fuel/air equivalence ratio (8). PM emissions are minimized during stoichiometric operation and increase for both rich and lean combustion (9). During cold start, SI engines use a rich fuel/air mixture, and particle number emission rates may be similar to modern diesels (1).

SI PM resembles diesel PM with respect to individual particles having complex shapes and consisting of a mixture of multiple chemical compounds (1, 9). A comprehensive knowledge of SI PM size, morphology, and composition is needed to characterize its physical, chemical, and toxic properties. The size and the structure of these particles is important as it influences their atmospheric transport properties, optical properties, and toxicological effects, for example, by controlling deposition, light scattering, and depth of penetration into the lung, respectively. Past research has focused on PM number emissions, mass emissions, and size distributions, and no studies of structural and fractal properties of SI PM are known to us.

The most common methods to characterize the complicated structure of agglomerate particles such as those emitted by SI and diesel engines are scanning electron microscopy (SEM) and transmission electron microscopy (TEM). SEM is typically used to investigate particle morphology and external structure, whereas TEM is typically used to examine the internal structure of the particles. Images taken with either of these two techniques can be analyzed to provide the projected two-dimensional (2-d) properties of agglomerate particles. From these 2-d properties of the agglomerates, actual 3-d structural properties can be derived including the mass-fractal dimension, which also provides useful insights into the agglomeration mechanism and volume equivalent size distribution of the particles.

The U.S. EPA and other sponsors conducted a program to characterize emissions of PM and other toxic components from randomly selected, light-duty SI vehicles in the Kansas City metropolitan area from July 2004 to March 2005. During this program, we collected PM emission samples from a few vehicles for the determination of particle structural and fractal properties.

SEM was used to investigate the morphology, agglomerate and monomer sizes, and shape of particles emitted from three light-duty vehicles with model years of 1991 and before. Energy-dispersive X-ray analysis was performed on the emitted PM to confirm its carbonaceous nature. Computer-aided analysis of the SEM images yielded the 3-d fractal dimension of the PM. Based on this observed fractal dimension of the particles, a growth mechanism for the agglomerates is identified. A number of 2-d structural properties of the agglomerates and their mathematical relations were determined. The shape of the particles was characterized using three conventional shape descriptors (10), aspect ratio, circularity (both sensitive to elongation), and root form factor (sensitive to boundary irregularity).

## 2. Experimental Section

**2.1. Sample Collection.** The vehicle emission tests were conducted in Kansas City during July to September 2004 (summer/round 1) and January to March 2005 (winter/round 2) using California's Unified Driving Cycle (UDC) that consists of a cold start phase 1, a more aggressive hot-stabilized phase 2, and a 10-min hot soak with the engine turned off, followed

\* Corresponding author e-mail: rajan@dri.edu.

† Current affiliation: Department of Physics, University of Nevada, Reno, NV.

‡ Current affiliation: Division of Engineering and Applied Sciences, Harvard University, Cambridge, MA.

§ Current affiliation: Droplet Measurement Technologies, Boulder, CO.

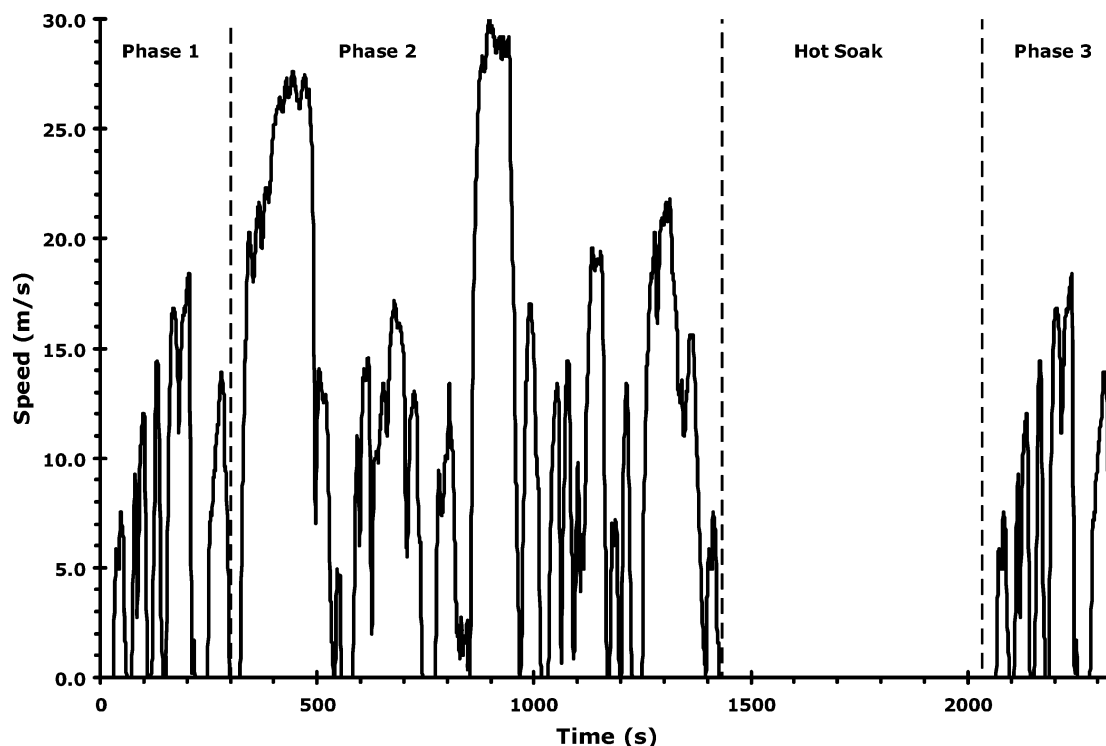


FIGURE 1. Prescribed vehicle speed as function of time for the three phases of California's unified driving cycle (UDC)

by a warm start phase 3 (repeat of phase 1). The prescribed UDC vehicle speed as function of time is shown in Figure 1. For the SEM analysis, filter samples were from three vehicles including one light-duty passenger vehicle (Buick Century; model year 1990; odometer reading 238 334 km; PM emission rates 12.9, 1.9, and 1.8 mg/km for UDC phases 1, 2, and 3) and two light-duty trucks (Chevrolet C2; model year 1973; odometer reading 91 974 km; PM emission rates 750, 249, and 42 mg/km for UDC phases 1, 2, and 3, and Chevrolet El Camino; model year 1976; odometer reading 98 894 km; PM emission rates 208, 10.3, and 2.1 mg/km for UDC phases 1, 2, and 3). Note that the odometer readings for the two light-duty trucks seem artificially low. This may be due to the odometers having turned over. A suite of instruments and samplers was operated to provide continuous PM analysis and to collect batch samples of particle and gaseous exhaust components for later analysis of their chemical and mass composition. For sampling exhaust particles to filters for SEM analysis, exhaust was first drawn from the exhaust pipe probe through insulated copper tubing to the constant volume sampler (CVS). A pump was used to draw diluted exhaust from the CVS through a PM<sub>2.5</sub> impactor, which eliminates particles larger than 2.5  $\mu\text{m}$  in diameter, onto nucleopore filters for SEM analysis. The flow rate through the nucleopore filter was adjusted to about 0.5 lpm to yield the appropriate filter loading for image analysis of individual agglomerates. While this estimate was correct for phase 3 of the UDC, phases 1 and 2 samples were overloaded and could only be analyzed for monomer size distribution but not for agglomerate properties. For phase 3, clean and well-defined images of around 200 agglomerates were selected for each vehicle and analyzed for particle shape, fractal dimension, agglomerate size distribution, monomer size distribution, and various projected properties. The selection of particles was based on the random distribution of particles on the SEM filter.

**2.2. Scanning Electron Microscopy (SEM) Analysis.** Particles were sampled on nucleopore clear polycarbonate filters, which were kept refrigerated and later prepared for SEM analysis by coating them with a 1-nm thick layer of

platinum to prevent charging during SEM analysis. The coated filters were analyzed using a field emission scanning electron microscope. SEM analysis may change the shape of particles through heat damage and physical damage. Heat damage evaporates semivolatile components from the filter due to the electron beam operating under vacuum conditions. Physical damage due to particle charging by the electron beam was avoided by keeping the accelerating voltages below 5 kV (11). Image analysis software (Digital Micrograph 3, Gatan Inc., and ImageJ, NIH) was used to quantify the structural properties of both the agglomerate particles and their monomer components. This analysis yields primary particle diameter  $d_p$  and primary particle projected area  $A_p$  for monomers and projected area  $A_a$ , maximum projected length  $L_{\text{max}}$ , and maximum projected width  $W_{\text{max}}$  (normal to  $L_{\text{max}}$ ) for agglomerates.

### 3. Results and Discussion

**3.1. Properties of Primary Particles.** Primary particles clearly distinguishable in agglomerates were selected, and their diameters were measured yielding primary particle size distributions corresponding to the three different phases of the UDC for the three vehicles. These primary particle size distributions can be reasonably approximated by lognormal distributions (Figure 2). As is evident from the figure, particles emitted during phases 1 and 3 of the UDC have very similar primary particle size distributions with count median diameters (CMD) between 30 and 40 nm and geometric standard deviations ( $\sigma$ ) between 1.11 and 1.38. Phases 1 and 3 follow an identical speed profile (Figure 1), and the differences in engine temperature and fuel/air equivalent ratio between phases 1 (cold start) and 3 (warm start) did not greatly change the monomer size distribution. The primary particle size distribution of the more aggressive speed profile of phase 2 can be represented using a bimodal lognormal distribution. The small mode has CMDs between 20 and 24 nm and geometric standard deviations  $\sigma$  between 1.17 and 1.23, while the large mode has CMDs between 54 and 60 nm and geometric standard deviations  $\sigma$  between 1.29 and 1.35. The higher and more variable engine load of phase 2

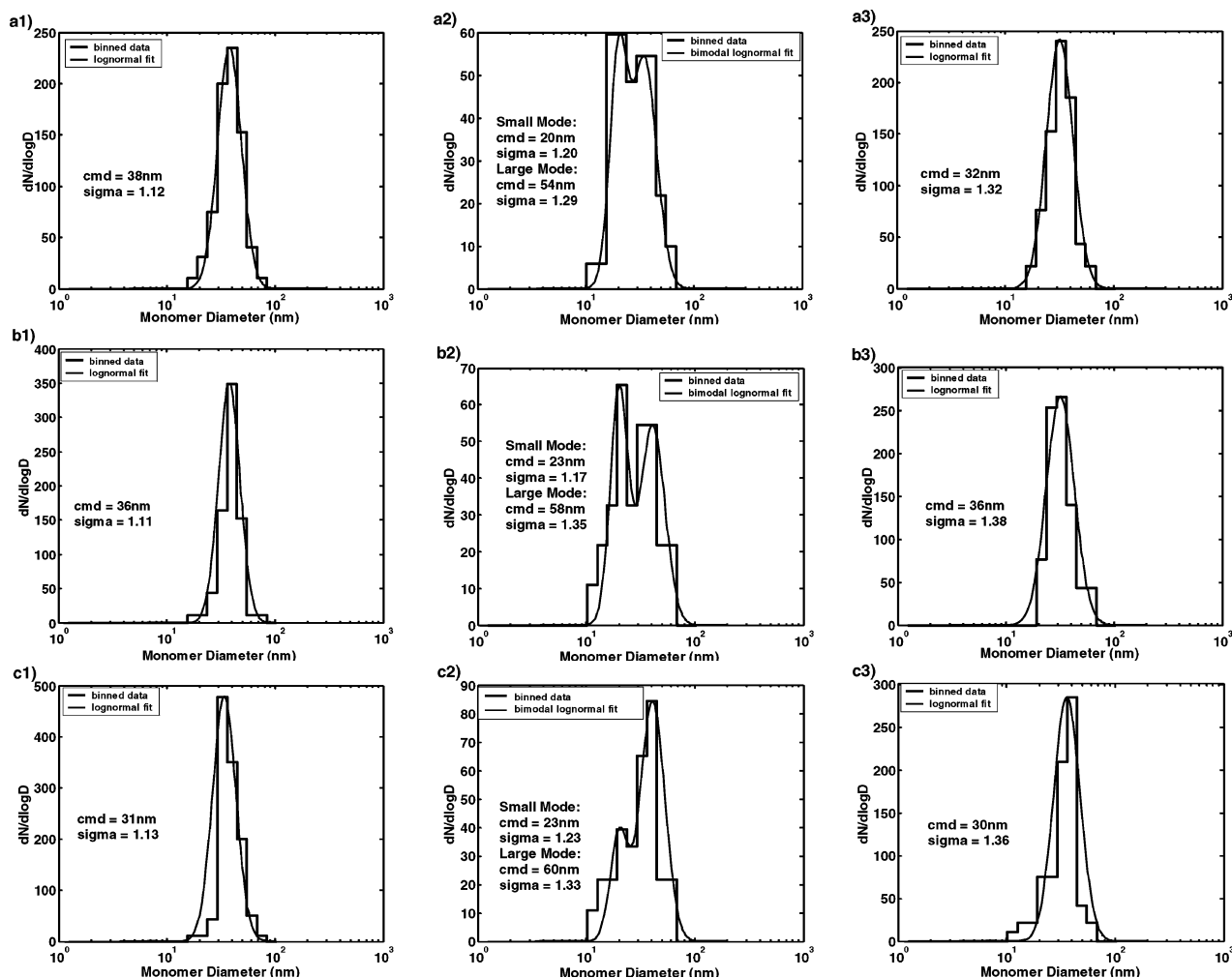


**FIGURE 2. Lognormal number size distributions of the monomers emitted by the (a) Buick Century, (b) Chevrolet C2, and (c) Chevrolet El Camino during phases 1, 2, and 3 of the UDC.**

(compared to phases 1 and 3) and associated changes in engine operating parameters (e.g., combustion temperature, rpm) yield primary particles with a larger size range than the less aggressive speed profile of phases 1 and 3. Unfortunately, not much is known about primary particle size as a function of combustion conditions, making it difficult to further interpret these results.

The primary particle size distributions measured here for SI vehicles during phase 1 and phase 3 of the UDC are very similar to the previously measured primary particle size distributions for diesel vehicles. Primary particle size distributions measured during phase 2 were bimodal with the small mode particles being smaller than diesel primary particles and the large mode particles being significantly larger. Lee et al. (12) measured primary particle diameters of diesel agglomerates and found that the mean primary particle diameter ranged from 28.5 to 34.4 nm with a nearly normal distribution. More recently, Park et al. (13) observed that the mean primary particle diameter of diesel agglomerates was 31.9 nm with a standard deviation of 7.2 nm.

**3.2. Partial Melting of Particles under Exposure to the SEM Electron Beam.** An important observation was made during SEM analysis of samples from phase 2 of the UDC. Upon exposing the agglomerates to the SEM electron beam with a relatively low accelerating voltage of 5 kV, some of them started to show increased area and reduced contrast within seconds of irradiation. We interpret this observation as partial melting (i.e., phase change from solid to liquid). Partial evaporation of the agglomerates may also occur but

would not explain the increased area observed. Figure 3 shows a temporal sequence of this process over a total of 15 s. This phenomenon of melting of carbonaceous aerosol particles upon exposure to a low voltage, accelerating electron has not been reported so far. The melting phenomenon was quantified using the change in Michelson contrast  $C$  of the SEM images (Figure 3) as function of time  $t$  with  $C$  defined as

$$C = \frac{G_{\text{particle}} - G_{\text{background}}}{G_{\text{particle}} + G_{\text{background}}} \quad (1)$$

where  $G_{\text{particle}}$  and  $G_{\text{background}}$  are the mean gray scale values of particle and background, respectively. The change in contrast of samples taken during phase 2 of the UDC is nearly linear in time as shown in Figure 4a, and the negative rate of contrast change (i.e.,  $-dC/dt$ ) can be used to quantify the melting phenomenon.

The negative rate of contrast change of our phase 2 samples is a near linear function of the organic carbon 1 (OC1) to elemental carbon (EC) ratio as determined by the thermal/optical reflectance (TOR) method (14) and shown in Figure 4b. Here OC1 is the OC fraction volatilized during the first temperature step of the thermal/optical analysis (14). Replacing OC1 with other OC fractions or with total OC resulted in a less linear relationship. Therefore, the near linear dependence of the negative rate of contrast change on the OC1/EC ratio may indicate that most of the organic com-

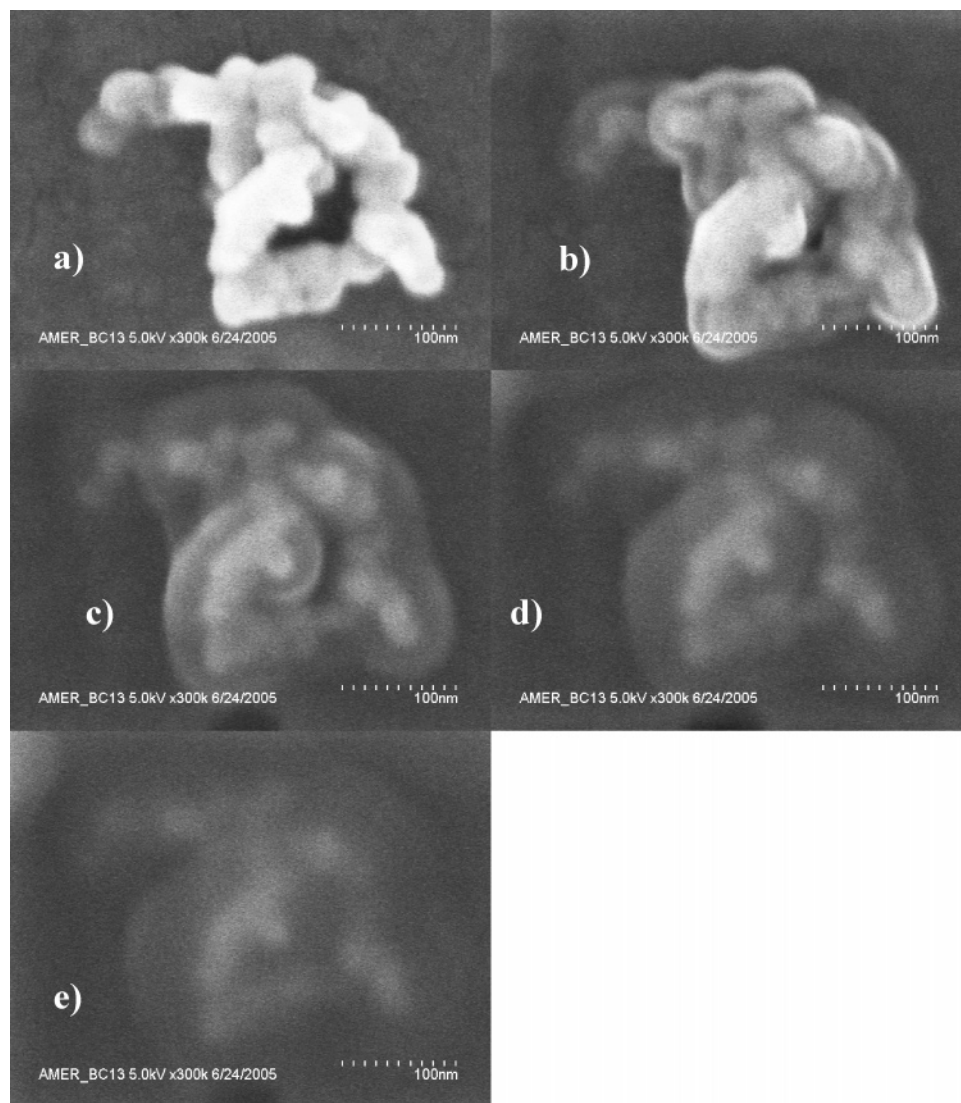


**FIGURE 3.** Sequential SEM snapshots taken during the melting of a particle sampled from a Chevrolet El Camino during phase 2 of the UDC. The particle was exposed to a low accelerating voltage beam of 5 kV for a total of 15 s. The melting indicates a high presence of organic carbon (OC).

pounds involved in the melting process are included in OC1. However, this observation is based on an extremely limited data set and will need to be corroborated with analysis of additional data.

**3.3. Projected (2-d) Properties of Spark Ignition Agglomerates.** SEM images of agglomerate particles were analyzed yielding the projected area equivalent diameter  $D$ , which is defined as the diameter of a circle with the same area as the projected particle (15). Rogak and Flagan (16) applied results of numerical calculations by Dahneke (17–19) to fractal aggregates and showed that for  $\text{TiO}_2$  and Si agglomerate particles with mobility diameters up to 400 nm, the projected area diameter is approximately equal to the mobility diameters  $D_{\text{mobility}}$ . Very recently, Park et al. (13) showed that this also applies to diesel agglomerates in the 50–220 nm mobility diameter range. More general, the relationship between the mobility diameter  $D_{\text{mobility}}$  and the projected area equivalent diameter  $D$  is well conserved in the transition regime as well as in the free molecular regime of the gas flow around the particle but breaks down in continuum flow regime (20). A recent study by Lee et al. (12) has shown that at atmospheric pressure, emissions from diesel vehicles lie mostly in the transition and free molecular regime. Based on their findings and taking into consideration the fact that the number density of SI particles is in general

much lower than that of diesel particles, we assume that the projected area equivalent diameter  $D$  of agglomerates from SI vehicles closely approximates their mobility diameter.

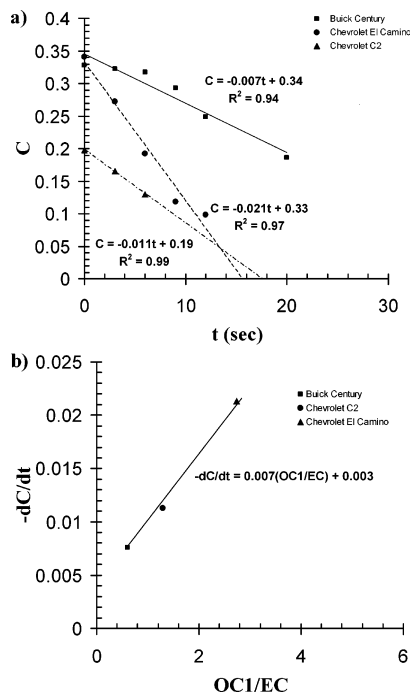
Most particles emitted by the three light-duty SI vehicles during phase 3 of the UDC can be classified as fine particles ( $D < 2.5 \mu\text{m}$ ), ultrafine particles ( $D < 0.10 \mu\text{m}$ ), or nanoparticles ( $D < 0.05 \mu\text{m}$ ), with most of the particle mass in the accumulation mode ( $0.10 \mu\text{m} < D < 0.3 \mu\text{m}$ ) (21). The number size distribution of these particles is shown in Figure 5, together with a fitted bimodal lognormal distribution. The small mode of this bimodal distribution consists of nonagglomerated single primary particles or very small, chained particles. It is however to be noted that the data represented in Figure 5 may not provide an accurate representation of the actual particle size number concentration emitted by the vehicles since only a subset of the emitted particles is collected onto the SEM filter.

Figure 6 shows for particles emitted by all three SI engines that the maximum length  $L_{\text{max}}$  scales to the projected area diameter  $D$ , a surrogate for the mobility diameter  $D_{\text{mobility}}$ , with a power law relationship as (13, 16)

$$L_{\text{max}} = kD^a \approx kD_{\text{mobility}}^a \quad (2)$$

where  $k$  is a proportionality constant, and  $a$  is the exponent





**FIGURE 4.** (a) Change in contrast  $C$  of SEM images as function of time  $t$  for emissions from three vehicles during phase 2 of the UDC and (b) the negative rate of change of  $C$  with time  $t$  (i.e.,  $-dC/dt$ ), which quantifies the rate of melting, is plotted as function of the organic carbon 1 (OC1) versus elemental carbon (EC) ratio yielding a near linear dependence.

characterizing the power law relationship. For the SI agglomerates studied here, the exponent  $a$  is between 1.22 and 1.28, which is comparable to a previously determined value of 1.26 for diesel agglomerates (13).

**3.4. Fractal Dimension of SI Agglomerates.** Since the introduction of the concept of fractal dimension by Mandelbrot (22), it has found significant use for describing the complex structures resulting from random aggregation of fine aerosol particles. In 3-d, the number  $N$  of fine particles aggregating to make up a cluster with fractal morphology scales with the radius of gyration  $R_g$  as (22)

$$N = k_g \left( \frac{2R_g}{d_p} \right)^{D_f} \quad (3)$$

where  $k_g$  is the fractal proportionality constant,  $d_p$  is the primary particle diameter, and  $D_f$  is the mass fractal dimension. For a given radius of gyration, the higher the fractal dimension, the higher is the number of primary particles in an agglomerate, thus resulting in a higher primary number or mass density.

In order to determine the 3-d mass fractal dimension of the agglomerates from the 2-d SEM images, one needs to have knowledge of the number of primary particles  $N$  and the radius of gyration  $R_g$  of the agglomerate. Empirical relationships between 2-d properties and 3-d properties are used to extract 3-d properties from the measured 2-d properties. The number of primary particles can be approximated as (23)

$$N = k_a \left( \frac{A_a}{A_p} \right)^\alpha \quad (4)$$

where  $A_a$  is the projected area of the agglomerate,  $A_p$  is the average projected area of primary particles,  $k_a$  is an empirical constant, and  $\alpha$  is an empirical exponent.

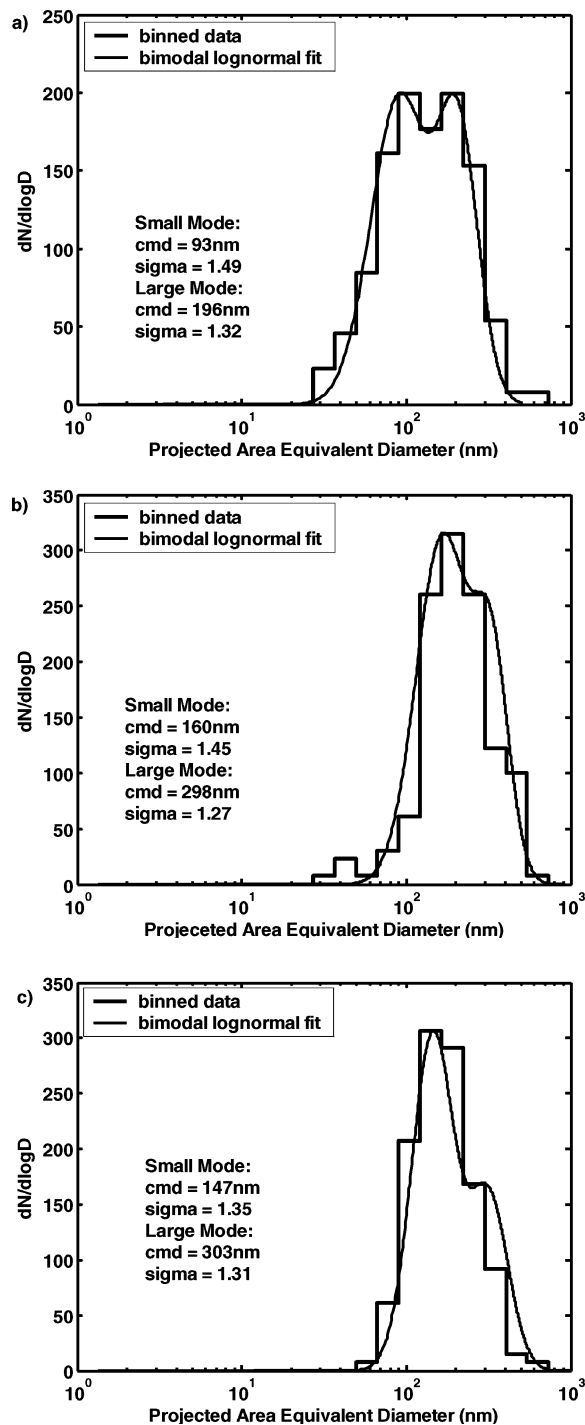


**FIGURE 5.** Projected area equivalent diameter  $D$  distribution for particle agglomerates emitted by the (a) Buick Century, (b) Chevrolet C2, and (c) Chevrolet El Camino during phase 3 of the UDC.

In addition, the estimation of  $N$  from  $A_a/A_p$  is sensitive to the value of the overlap parameter, which is defined for spherical particles as the ratio of the primary particle diameter to the distance between the centers of two touching particles. Oh and Sorensen (23) took the overlap of primary particles into account and determined  $k_a$  and  $\alpha$  as function of overlap parameter. In our study, these values of  $\alpha$  and  $k_a$  are employed when using eq 4 to determine the number of primary particles in the agglomerates. The overlap parameter for most of the SI particles studied here is between 1.45 and 1.5. This high overlap parameter can be attributed to the OC that fills the gaps between the near spherical EC cores of the primary particles (Figure 3).

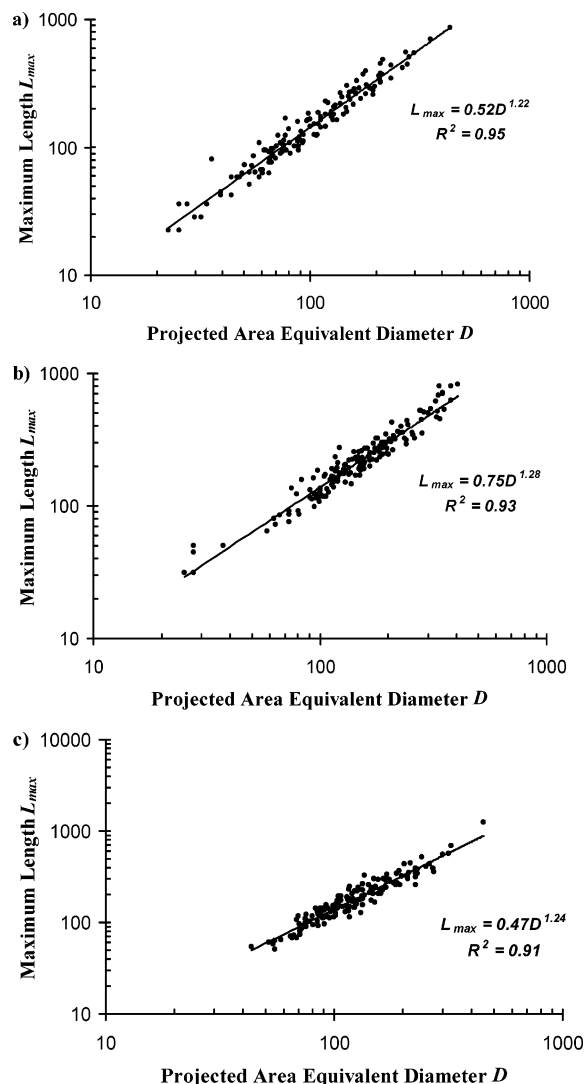


**FIGURE 6.** Relationship between the maximum projected length  $L_{\max}$  and projected area equivalent diameter  $D$  for particle agglomerates emitted by the (a) Buick Century, (b) Chevrolet C2, and (c) Chevrolet El Camino during phase 3 of the UDC.

The radius of gyration  $R_g$ , a 3-d parameter, can also be extracted from projected properties. Previous studies suggested that the maximum projected length  $L_{\max}$  could be used as a substitute of  $R_g$  (i.e.,  $L_{\max}/2R_g = \text{constant}$ ) (24–26). Oh and Sorensen (23) found that  $L_{\max}/2R_g = 1.45$ , while Brasil et al. (26) determined  $L_{\max}/2R_g = 1.50$ . Here, we use the value reported by Brasil et al. (26) yielding the fractal dimension  $D_{fL}$  based on the maximum projected length  $L_{\max}$  as

$$N = k_L \left( \frac{L_{\max}}{d_p} \right)^{D_{fL}} \quad (5)$$

where  $d_p$  is the primary particle diameter, and  $k_L$  is the proportionality constant. The two fractal dimensions  $D_{fL}$  (based on maximum projected length) and  $D_f$  (based on radius of gyration  $R_g$ ) have identical values and can be used interchangeably, while the proportionality constants  $k_g$  and  $k_L$  are different and related as

$$k_L = k_g \left( \frac{2R_g}{L_{\max}} \right)^{D_{fL}} = k_g \left( \frac{2R_g}{L_{\max}} \right)^{D_f} \quad (6)$$

Fractal dimensions  $D_{fL}$  of agglomerates emitted from the three SI vehicles calculated with eq 5 are shown in Figure 7.

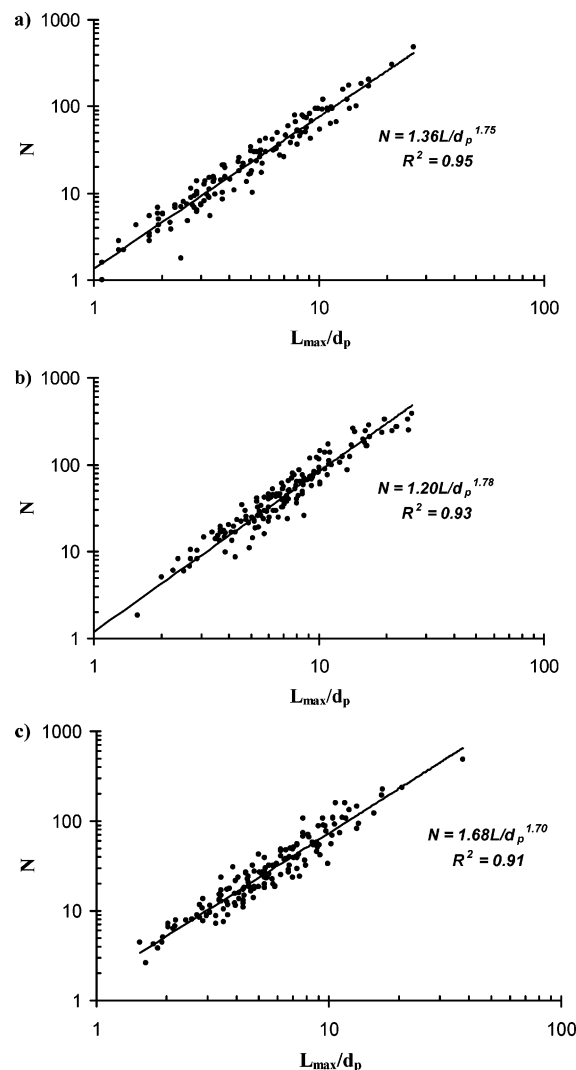


**FIGURE 7.** Fractal dimension  $D_{fL}$  calculated using eq 6 for particle agglomerates emitted by the (a) Buick Century, (b) Chevrolet C2, and (c) Chevrolet El Camino during phase 3 of the UDC.

The maximum projected length  $L_{\max}$  is obtained by direct measurement, while  $N$  is determined from eq 4 using values for  $\alpha$  of 1.20, 1.14, and 1.16 and for  $k_a$  of 1.50, 1.30, and 1.35 for the Buick Century, Chevrolet C2, and Chevrolet El Camino, respectively (23). As can be seen from Figure 7, the values of the 3-d fractal dimension of these SI agglomerates are between 1.7 and 1.78. This range for the 3-d fractal dimension of SI agglomerates is overlapping with, but somewhat lower than, that of 1.75–1.88 for diesel agglomerates (12, 13) and within the range of 1.67–1.83 for particles emitted from the combustion of biomass fuels (11).

The 3-d fractal dimension of the SI agglomerates (i.e., 1.7–1.78) indicates a diffusion-limited cluster–cluster aggregation mechanism for the agglomerate formation (27, 28), which has also been proposed for the formation of diesel agglomerates (12).

**3.5. Shape Analysis of SI Agglomerates.** Although shape is an inherently three-dimensional attribute and can be defined in many different ways, many characterization techniques use two-dimensional data to define them (29). These “conventional shape descriptors” combine two measures of particle size as a ratio (10). Three simple shape descriptors were selected for our analysis, that is aspect ratio (AR) (sensitive to elongation), root form factor (RFF) (sensitive to boundary irregularity), and roundness (RN) (sensitive to elongation). Using a combination of ImageJ and Digital

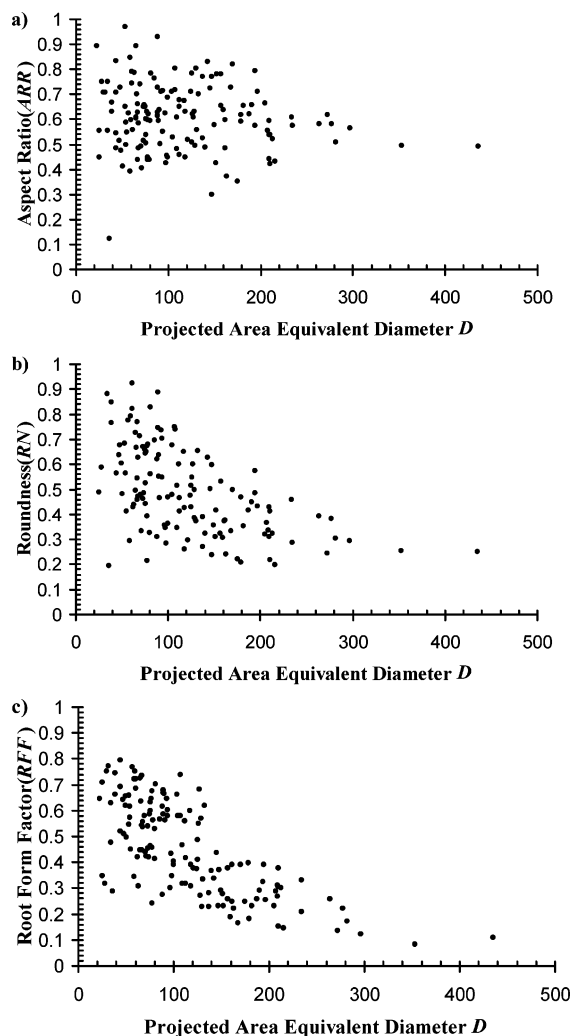


**FIGURE 8.** Relationship between the projected area equivalent diameter with (a) aspect ratio (ARR), (b) root form factor (RFF), and (c) roundness (RN) for particles emitted by the Buick Century during phase 3 of the UDC.

Micrograph 3 software, these shape descriptors were calculated from the maximum projected width  $W_{\max}$ , maximum projected length  $L_{\max}$ , projected area  $A_a$ , and perimeter length  $P$  of the individual aggregates as

$$AR = \frac{W_{\max}}{L_{\max}} \quad (7)$$

$$RFF = \frac{\sqrt{4\pi A_a}}{P} \quad (8)$$

and

$$RN = \frac{4A_a}{\pi L_{\max}^2} \quad (9)$$

For particles emitted during phase 3 of the UDC from a Buick Century (light-duty vehicle, 1991 model year), these shape descriptors are shown as a function of the corresponding projected area equivalent diameter  $D_{\text{Projected}}$  in Figure 8. For small diameters, the aspect ratio (AR) is quite varied with large values approaching 1, which corresponds to a rather circular structure. As the diameter of the particle increases, both the variability and the value of the aspect ratio are reduced, indicating the formation of more lengthy

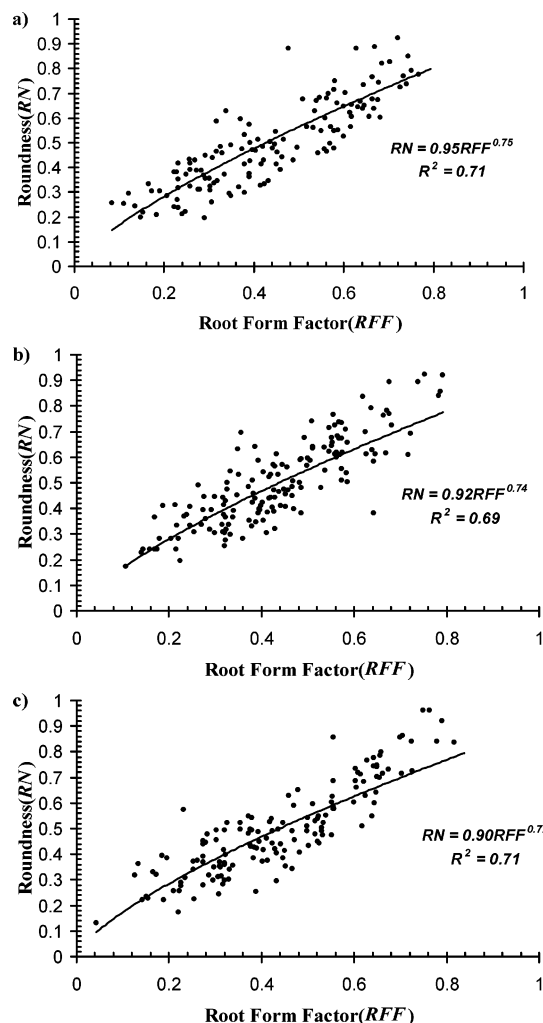


**FIGURE 9.** Relationship between the root form factor (RFF) and roundness (RN) for particle agglomerates emitted by the (a) Buick Century, (b) Chevrolet C2, and (c) Chevrolet El Camino during phase 3 of the UDC.

chainlike agglomerates. A similar, but more pronounced, observation can be made for the particle roundness decreasing in value and variability with increasing diameter, again indicating more elongated particles at large sizes. The root form factor (RFF) of the particles also behaves similarly to the aspect ratio and roundness of the particles. The decrease in RFF with increasing diameter implies increasing boundary irregularity of the particles corresponding to the random positioning of small clusters and monomers constituting the chainlike agglomerates. A similar pattern of decreasing ARR, RF, and RN with increasing diameter was observed for agglomerates emitted by all three vehicles tested.

The relationship between the root form factor (RFF) and the roundness (RN) of the particles emitted from the three SI vehicles is shown in Figure 9 and can be described as a power law relationship with an average exponent of 0.74 as

$$RN = RFF^{0.74} \quad (10)$$

## Acknowledgments

It is a pleasure to thank Dr. Eric M. Fujita and Mr. David Campbell for facilitating our participation in the Kansas City emission study and Dr. Barbara Zielinska for insightful discussions. This work was funded in part by the Desert Research Institute's VPR Research Enhancement Program and Institutional Project Assignment Program and by the

## Literature Cited

- (1) Kittelson, D. B. Engines and nanoparticles: A review. *J. Aerosol. Sci.* **1998**, 29 (5-6), 575–588.
- (2) Vedal, S. Critical review: Ambient particles and health: Lines that divide. *J. Air Waste Manage. Assoc.* **1997**, 47 (5), 551–581.
- (3) Haywood, J. M.; Ramaswamy, V. Global sensitivity studies of the direct radiative forcing due to anthropogenic sulfate and black carbon aerosol. *J. Geophys. Res.* **1998**, 103 (D6), 6043–6058.
- (4) Watson, J. G. 2002 Critical review – Visibility: Science and regulation. *J. Air Waste Manage. Assoc.* **2002**, 52 (6), 626–713.
- (5) Finlayson-Pitts, B. J.; Pitts, J. N. *Chemistry of the upper and lower atmosphere: Theory, experiments, and applications*; Academic Press: San Diego, CA, 2000.
- (6) Gertler, A. W. Diesel vs. Gasoline emissions: Does PM from diesel or gasoline vehicles dominate in the U.S.? *Atmos. Environ.* **2005**, 39 (13), 2349–2355.
- (7) Maricq, M. M.; Podsiadlik, D. H.; Chase, R. E. Gasoline vehicle particle size distributions: Comparison of steady state, FTP, and US06 measurements. *Environ. Sci. Technol.* **1999**, 33 (12), 2007–2015.
- (8) Tobias, H. J.; Beving, D. E.; Ziemann, P. J.; Sakurai, H.; Zuk, M.; McMurry, P. H.; Zarling, D.; Waytulonis, R.; Kittelson, D. B. Chemical analysis of diesel engine nanoparticles using a nano-DMA/thermal desorption particle beam mass spectrometer. *Environ. Sci. Technol.* **2001**, 35 (11), 2233–2243.
- (9) Kayes, D.; Hochgreb, S. Mechanisms of particulate matter formation in spark-ignition engines. 2. Effect of fuel, oil, and catalyst parameters. *Environ. Sci. Technol.* **1999**, 33 (22), 3968–3977.
- (10) Hentschel, M. L.; Page, N. W. Selection of descriptors for particle shape characterization. *Part. Part. Syst. Charact.* **2003**, 20 (1), 25–38.
- (11) Chakrabarty, R. K.; Moosmüller, H.; Garro, M. A.; Arnott, W. P.; Walker, J. W.; Susott, R. A.; Babbitt, R. E.; Wold, C. E.; Lincoln, E. N.; Hao, W. M. Emissions from the laboratory combustion of wildland fuels: Particle morphology and size. *J. Geophys. Res.* **2006**, 111. doi:10.1029/2005jd006659.
- (12) Lee, K. O.; Cole, R.; Sekar, R.; Choi, M. Y.; Kang, J. S.; Bae, C. S.; Shin, H. D. Morphological investigation of the microstructure, dimensions, and fractal geometry of diesel particulates. *Proc. Combust. Inst.* **2002**, 29, 647–653.
- (13) Park, K.; Kittelson, D.; McMurry, P. Structural properties of diesel exhaust particles measured by transmission electron microscopy (TEM): Relationships to particle mass and mobility. *Aerosol Sci. Technol.* **2004**, 38 (9), 881–889.
- (14) Chow, J. C.; Watson, J. G.; Pritchett, L. C.; Pierson, W. R.; Frazier, C. A.; Purcell, R. G. The DRI thermal/optical reflectance carbon analysis system: Description, evaluation and applications in U.S. air quality studies. *Atmos. Environ.* **1993**, 27A (8), 1185–1201.
- (15) Hinds, W. C. *Aerosol technology*, 2nd ed.; Wiley-Interscience: New York, 1999.
- (16) Rogak, S. N.; Flagan, R. C.; Nguyen, H. V. The mobility and structure of aerosol agglomerates. *Aerosol. Sci. Technol.* **1993**, 18 (1), 25–47.
- (17) Dahneke, B. E. Slip correction factors for nonspherical bodies - 1. Introduction and continuum flow. *J. Aerosol. Sci.* **1973**, 4 (2), 139–145.
- (18) Dahneke, B. E. Slip correction factors for nonspherical bodies - 2. Free molecule flow. *J. Aerosol. Sci.* **1973**, 4 (2), 147–161.
- (19) Dahneke, B. E. Slip correction factors for nonspherical bodies - 3. The form of the general law. *J. Aerosol. Sci.* **1973**, 4 (2), 163–170.
- (20) DeCarlo, P. F.; Slowik, J. G.; Worsnop, D. R.; Davidovits, P.; Jimenez, J. L. Particle morphology and density characterization by combined mobility and aerodynamic diameter measurements. Part I: Theory. *Aerosol. Sci. Technol.* **2004**, 38 (11), 1185–1205.
- (21) Seinfeld, J. H.; Pandis, S. N. *Atmospheric chemistry and physics: From air pollution to climate change*; Wiley: New York, 1998.
- (22) Mandelbrot, B. B. *The fractal geometry of nature*; W.H. Freeman: San Francisco, CA, 1982.
- (23) Oh, C.; Sorensen, C. M. The effect of overlap between monomers on the determination of fractal cluster morphology. *J. Colloid Interface Sci.* **1997**, 193 (1), 17–25.
- (24) Samson, R. J.; Mulholland, G. W.; Gentry, J. W. Structural analysis of soot agglomerates. *Langmuir* **1987**, 3 (2), 272–281.
- (25) Köylü, Ü. Ö.; Faeth, G. M.; Farias, T. L.; Carvalho, M. G. Fractal and projected structure properties of soot aggregates. *Combust. Flame* **1995**, 100 (4), 621–633.
- (26) Brasil, A. M.; Farias, T. L.; Carvalho, M. G. A recipe for image characterization of fractal-like aggregates. *J. Aerosol. Sci.* **1999**, 30 (10), 1379–1389.
- (27) Meakin, P. Cluster-particle aggregation with fractal (Levy flight) particle trajectories. *Phys. Rev. B* **1984**, 29 (6), 3722–3725.
- (28) Jullien, R.; Botet, R. *Aggregation and fractal aggregates*; World Scientific: Singapore, 1987.
- (29) Stachowiak, G. W.; Podsiadlo, P. Characterization and classification of wear particles and surfaces. *Wear* **2001**, 249 (3), 194–200.

Received for review March 7, 2006. Revised manuscript received July 7, 2006. Accepted August 3, 2006.

ES060537Y